

Exciton Condensation in an Atomically-thin MoS₂ Semiconductor

Qihua Xiong (✉ qihua_xiong@tsinghua.edu.cn)

Tsinghua University <https://orcid.org/0000-0002-2555-4363>

Andres Granados del Aguila

Yi Wong

Nanyang Technological University

Xue Liu

Anhui University

Antonio Fieramosca

Nanyang Technological University <https://orcid.org/0000-0002-8912-1137>

T. Thu Ha Do

Nanyang Technological University

Marco Battiato

Nanyang Technological University <https://orcid.org/0000-0002-1902-2272>

Physical Sciences - Article

Keywords: excitons, electrostatic doping, atomically-thin MoS₂ semiconductor

Posted Date: October 1st, 2021

DOI: <https://doi.org/10.21203/rs.3.rs-940264/v1>

License:  This work is licensed under a Creative Commons Attribution 4.0 International License.

[Read Full License](#)

Exciton Condensation in an Atomically-thin MoS₂ Semiconductor

Andrés Granados del Águila,^{1†*} Yi Ren Wong,^{1†} Xue Liu², Antonio Fieramosca¹, T. Thu Ha Do¹, Marco Battiato¹, Qihua Xiong^{3,4*}

¹*Division of Physics and Applied Physics, School of Physical and Mathematical Sciences, Nanyang Technological University, 637371, Singapore.*

²*Institutes of Physical Science and Information Technology, Anhui University, Hefei, China.*

³*Beijing Innovation Center for Future Chips, Tsinghua University, Beijing 100084, China.*

⁴*Beijing Academy of Quantum Information Sciences, Beijing 100193, China.*

† These authors contributed equally to this work.

* To whom correspondence should be addressed:

qihua_xiong@tsinghua.edu.cn ; a.granadosdelaguila@ntu.edu.sg

Condensation of a dilute Bose gas of excitons (coupled electron-hole pairs) in a direct-bandgap semiconductor was first theoretically predicted in 1968¹. This exotic state of matter is expected to exhibit spectacular non-linear properties, such as superradiance and superfluidity. However, direct experimental observation of condensation of optically-active excitons in conventional semiconductors has been hindered by their short lifetimes and weak collective excitonic interactions. Here, we have experimentally realized the condensation of short-lived excitons in a *direct-bandgap*, atomically-thin MoS₂ semiconductor. The signature is the anomalous transport of the fast-expanding exciton density, originating from a thermalized dilute gas generated under the laser spot. Below the critical temperature $T_c \sim 150$ K, the exciton liquid propagates over ultra-long distances (at least 60

micrometers) with record speed in a solid-state system of $\sim 1.8 \times 10^7$ m/s ($\sim 6\%$ the speed of light), fuelled by the unconventionally strong repulsions among excitons. The condensation is controlled by many-body interactions in the gas mixture of excitons (bosons) and free-carriers (fermions) via an electrical backgate. Our results demonstrate electrostatic doping as a simple approach for the investigation of correlated states of matter at high-temperatures, excitonic circuitry and spin-valley Hall devices mediated by exciton superfluids in semiconducting monolayers.

Similar to ultracold atomic gases^{2,3}, a dilute gas of excitons optically injected in a semiconductor below a critical temperature (T_c) is well-described as a weakly interacting Bose gas that can spontaneously condense (in momentum space) into a liquid, via many-body repulsive interactions among electron-hole pairs^{1,4}. Despite the efforts over the last five decades, experimental observation of condensation of optically-active (short-lived) excitons in direct-bandgap semiconductors has not been realized. To stabilize the condensate in these systems, the repulsive interactions among excitons must compensate the fast decay of the population. Furthermore, the formation of other complexes via attractive forces, such as charged states (trions), molecules (biexcitons) or even electron-hole droplets⁵, are competing effects against exciton condensation. To overcome the limitations in direct-bandgap semiconductors with weakly-interacting excitons, top-down approaches have been taken. For instance, by using microcavities, polaritons with ultra-light effective masses are obtained, allowing for metastable Bose condensation at high densities⁶. Alternatively, quantum fluids have been reported in double quantum-wells (DQWs) by using optically-forbidden (long-lived) dipolar excitons, whose electron and holes resides in opposite QW layers (spatially-indirect)⁷⁻¹³. In DQWs, the long lifetimes and the tailored repulsive interactions among indirect dipolar excitons drive the condensation.

Excitons in direct-bandgap two-dimensional semiconductors, such as monolayer transi-

tion metal dichalcogenide (TMD) MoS₂, have short lifetimes and stable exciton complexes^{14–16}, which a priori may preclude the formation of exciton liquids. Here, by using spatially-, time- and energy-resolved photoluminescence (PL) and reflectivity measurements, we have experimentally realized the condensation of a dilute exciton gas in MoS₂ monolayer until $T_c \sim 150$ K, evidenced by the anomalous transport over long distances of at least 60 μm (limited by the sample size) with record speed in a solid-state system of $\sim 1.8 \times 10^7$ m/s ($\sim 6\%$ the speed of light). The condensation is driven by unconventionally strong repulsive interactions among excitons, directly revealed by ~ 3 meV blueshift of the exciton energy. We also present the phase diagram by using an electrical backgate and temperature as relevant thermodynamic parameters that control the interplay between attractive (exciton-electron) and repulsive (exciton-exciton) many-body interactions present in the Bose-Fermi gas mixture in the monolayer semiconductor.

In our PL imaging experiments, we used a laser as excitation source with a well-defined Gaussian spatial distribution with full width at half-maximum (fwhm) of $\sigma_{\text{Laser}} \sim 1.5 \mu\text{m}$. By using near-resonant excitation (Fig. 1(A)), a low density gas of excitons (up to $n_X \sim 1.1 \times 10^{10} \text{ cm}^{-2}$, well below the Mott density¹⁷ $n_{\text{Mott}} \sim 10^{13} \text{ cm}^{-2}$) is photogenerated with minimal momentum ($\hbar k_X \sim 0$), kinetic energy ($E_X(k_X) = E_g + \hbar k_X^2 / 2m_X^*$) and group velocity ($v_X(k_X) = \partial E_X / (\hbar \partial k_X)$), where \hbar is reduced Planck constant and m_X^* is exciton effective mass. In this way, the exciton gas reaches thermal equilibrium with the semiconductor lattice right after photoexcitation ($E_X(k_X) - E_X(0) \sim k_B T$, where k_B is the Boltzmann constant and T is temperature), persisting within the radiative lifetime of the state.

Monolayer MoS₂ has large intrinsic concentration of electrons that markedly affects the optical response of the two-dimensional semiconductor. We control the electron density (n_e) and enhance the excitonic response in our samples by incorporating a backgate (V_g). At large positive V_g (*i.e.*, high n_e), the reflectance contrast in Fig. 1(B) is dominated by a single reso-

nance, denoted as X^- , that corresponds to the so-called charged exciton or trion state, or also described as attractive polaron. In this metallic regime ($V_g > 20$ V), the neutral exciton, also referred to as repulsive polaron, is absent. Decreasing V_g (lower n_e), the excitonic resonance X starts appearing at 38 meV above X^- . A further decrease in V_g leads to a strong increase in the exciton absorption and a monotonic shift to lower energies. The X^- feature disappears below $V_g = -30$ V. At this insulating regime ($V_g < -30$ V), only the neutral exciton resonance ($E_X(0) \sim 1.950$ eV) is resolved.

The change in the character from metallic to insulating of the MoS₂ monolayer drives an instability in the excitonic system that results in an anomalous excitonic transport and non-linear optical effects. Therefore, to accurately study this, we have produced high-quality large area ($A \sim 1200 \mu\text{m}^2$) MoS₂ monolayers. The longest dimensions of our samples of 40-60 μm (Fig. 1(C) and Figs. S4-S6) are 30-40 times larger than σ_{Laser} that allows us to monitor the long-range propagation and distribution of the exciton population in space via PL imaging as a function of V_g , power and temperature.

The low-temperature ($T = 20$ K) PL emission at $V_g = 0$ V is localized around the laser spot, positioned at the center of the sample (Fig. 1(D)). Remarkably, maintaining the same excitation conditions but setting $V_g = -60$ V, we observe light-emission with homogeneous intensity distribution over the entire crystal (Fig. 1(E)) outside the laser spot. Such PL profile suggests that excitons have homogeneously spread over large distances away from the excitation source (see Fig. S5 for reproducibility in other devices). Given the negligible kinetic energy and low mobility of the exciton gas¹⁸⁻²⁴, such a long-range transport is striking and has not been theoretically predicted for TMDs.

For a fixed power ($P = 1000 \mu\text{W}$) and temperature ($T = 20$ K), the sudden changes in the spatial profile on the light-emission with varying V_g can be seen in the Supporting Video,

while PL image cross sections are shown in Fig. 2(A). When V_g decreases from 0 to -20 V, the PL intensity profile remains unchanged and exhibits a bimodal distribution. Most of the PL intensity ($\sim 75\%$) follows a Gaussian distribution centred at the excitation spot ($x_{\text{Laser}} = 0 \mu\text{m}$). The Gaussian profile (region-I) indicates diffusive transport of the exciton gas away from the generation source. The fwhm at region-I $\sigma_I = (1.6 \pm 0.2) \mu\text{m}$ is comparable to σ_{Laser} and manifest the low mobility of a non-interacting exciton gas in TMDs¹⁸⁻²⁴. The shape of this distribution remains unaffected upon variations of V_g , P and T (Fig. 2(A)-(C)).

The PL profiles exhibit a tail that extends further into the sample beyond region-I, which suggests a weakly interacting exciton gas at $V_g = 0$ V. Its intensity follows an exponential distribution (region-II). Intriguingly, when decreasing V_g , the amplitude and decay length (L_X) of the exponential distribution increase nonlinearly (Figs. S7-S8). In particular, at $V_g = 0$ V, region-II represents the $\sim 25\%$ of the PL intensity that ultimately increases to $\sim 90\%$ at $V_g = -60$ V. The acquired quasi-homogeneous intensity of the PL profile at large negative voltages (limited by the finite size of the crystal), typically observed in condensed polaritons, indicates ballistic-like transport over micrometer distances of the short-lived excitons in monolayer MoS₂.

Moreover, the PL pattern at region-II also varies non-linearly with excitation power as shown by Fig. 2(B) at $V_g = -60$ V and $T = 20$ K. With increasing power, the exponential decay becomes longer and asymptotically approaches a step-like shape at the highest injected exciton density. Remarkably, keeping $P = 1000 \mu\text{W}$ and $V_g = -60$ V, the step-like profile is observed until exceptionally high lattice temperatures of ~ 150 K (Fig. 2(C)). Further increase of T leads to a rapid decay of the exponential component of the PL profile that becomes negligible (<10%) above 180 K (Fig. S6).

Such striking instabilities of the excitonic density in region-II are attributed to a thermodynamic phase transition, where a fraction of the dilute gas of excitons has spontaneously

condensed into a liquid. The formation of the exciton liquid is revealed by the anomalous transport behaviour imprinted in the exponential PL distribution. Therefore, we use the exponential decay constant (L_X), defining the transport length of the exciton fluid, as a characteristic macroscopic parameter to closely monitor the phase transition, which originates from microscopic many-body interactions, as a function of V_g , P and T .

The phase diagram of $L_X (V_g, T)$ is shown in Figure 2(D) for $P = 1000 \mu\text{W}$. The liquid phase domain (left-side of the dashed guideline) shows the largest transport length (up to $L_X = (64 \pm 3) \mu\text{m}$) that extends until $V_g = -30 \text{ V}$ and high-temperature of $\sim 150 \text{ K}$, abruptly shortening by one-order-of magnitude ($L_X = (5 \pm 4) \mu\text{m}$) when entering the gas phase (right-side of the dashed guideline). Intriguingly, exciton condensation occurs even with low excitation power provided that the temperature and the electron density are low enough (Fig. S9). Unlike in conventional phase diagrams for indirect excitons²⁵, here in the case of direct excitons in MoS₂ monolayer, V_g is an important parameter, because the fraction of the exciton gas that condenses depends critically on the electron density present in the two-dimensional semiconductor. The liquid phase is observed only when monolayer MoS₂ approaches the insulating regime (Fig. 1(B)).

Microscopically, what distinguishes the exciton liquid from the gas is the competition between repulsive (exciton-exciton) and attractive (exciton-electron) interactions within the mixture of excitons (boson) and electrons (fermion) (illustration Fig. 2(D)). In the gas phase, the short transport length suggests that excitons are spatially localized by the strong attractive interactions induced by the dense electron gas. In this metallic-like regime, the many-body repulsive exciton-exciton interactions required for their condensation are screened, regardless of the exciton density, which implies attractive forces are dominant to the leading order $n_e/n_X > 1$.

Nominally, interactions between electrons and excitons remain attractive for all n_e ²⁶,

which prevents for the formation of the exciton liquid. The short-range attractive interactions reduce when gradually decreasing n_e to become smaller, or of order of n_X ($n_e/n_X \leq 1$). In the insulating regime, the low electron density (*i.e.*, negligible screening) allows for the repulsive exciton-exciton interactions²⁷ to take over, giving rise to the spontaneous condensation of the dilute exciton gas.

Moreover, the fraction of condensed excitons is also markedly affected by temperature. Given the large binding energy of MoS₂ excitons, we estimate that the density of thermally excited electrons surpasses n_X at $T = (160 \pm 40)$ K (Fig. S12). This range of temperatures depends on the intrinsic carrier concentration and agrees well with the gas-to-liquid phase transition. The critical exciton condensation temperature ($T_c \sim 150$ K) observed here for direct-bandgap MoS₂ monolayer is much higher than that for superfluid helium (2.17 K), indirect excitons in III-V DQWs (<10 K)^{7-9,11,25}, III-V and II-VI polaritons⁶ (<20 K) and Cu₂O excitons²⁸ (<1 K) and is similar to the estimated temperature for tightly-bound indirect excitons in TMD DQWs²⁹. The remarkably high- T_c suggests unusually strong repulsions between excitons occupying the lowest-energy state and sets a record for condensation and achievement of exciton superfluidity in direct-bandgap semiconductors.

The macroscopic expansion of the exciton liquid in the atomically-thin MoS₂ surface causes the up to three-orders-of magnitude increment of the integrated PL intensity with decreasing V_g (Fig S10-11) that explains for the near-unity PL quantum yield reported in neutral MoS₂ samples^{30,31}. Such giant PL enhancement, or superradiance, indicates that light-emission of the liquid originates from optically-active (bright) excitons. Therefore, the long-range propagation of excitons within their ultra-short radiative lifetime, typically $\tau_X \sim 1\text{-}20$ ps in TMDs¹⁴⁻¹⁶, strongly suggests the unconventionally high-speed of the exciton fluid because $L_X(T, V_g) = v_{X,L}(T, V_g) \cdot \tau_X$.

We demonstrate the ultrafast transport by performing spatially- and energy-resolved pump-

probe reflectance measurements with 150-femtosecond time-resolution. A broadband-energy source (probe) illuminates the entire MoS₂ crystal, while the single-frequency beam (pump) excites the center of the sample ($x = 0 \mu\text{m}$) with a reduced beam size of $\sigma_{\text{Laser}} \approx 2 \mu\text{m}$. The pump, tuned near the exciton resonance, generates an exciton gas with estimated density $n_X \sim 1.7 \times 10^{12} \text{ cm}^{-2}$ under the laser spot. After gas thermalization, as excitons condense via repulsive interactions, they are propelled away from the generation source, altering the spatial-dependence of the intensity and energy distribution of the reflectance profile through the monolayer.

Figure 3 shows the differential reflectance signal $DR(x, E)$ at $V_g = -60 \text{ V}$ for representative delay times (Δt) between pump and probe. At $\Delta t = 0 \text{ ps}$ (Fig. 3(A)) defined as the time frame at which the photogenerated density under the laser spot is thermalized at the exciton resonance energy, a weak positive DR signal (photobleaching) arise from the exciton population at $E_X(0) = 1.950 \text{ eV}$. Increasing Δt , the photobleaching feature becomes pronounced and extends through space (Fig. 3(B)-(D)), reaching $20 \mu\text{m}$ in just 1.2 ps . On the other hand, other states at energies below X do not propagate proving that the long-range transport observed in Figures 1 and 2 is entirely determined by excitons, which is further supported by the suppression of the propagation when n_e is high at $V_g = 0 \text{ V}$ (Fig. S15). These observations have been reproduced in multiple devices (Fig. S16).

Figure 4(A) shows the time-dependence of the mean-square displacement (MSD) $\sigma_{\text{II}}^2 - \sigma_{\text{II},0}^2$, where $\sigma_{\text{II},0}^2$ is the fwhm at $\Delta t = 0 \text{ ps}$. Similarly to ballistic transport, the MSD in the liquid phase (circles) scales super-linearly with increasing time, which is in clear contrast to the linear trend at the gas phase (squares) that is characteristic of diffusive transport. Analysis of the MSD with an parabolic function (solid-line) provides the velocity at which the exciton liquid expands

over the atomically-thin semiconducting layer, which is $v_{X,L} = (1.8 \pm 0.3) \times 10^7$ m/s.

The obtained velocity is exceptionally high, being only 6% the speed of light (3×10^8 m/s). Remarkably, $v_{X,L}$ is one-order-of magnitude larger than condensed polaritons in ultra-high quality micro-cavities in III-V^{6,32}, ZnO³³, than the Fermi velocity of Dirac electrons in graphene^{34,35} and in metals ($v_F \approx 10^6$ m/s) and than ballistic excitons in perovskites semiconductors^{36,37}, three orders of magnitude larger than excitons fluids in III-V single³⁸ and DQWs⁷, in Cu₂O³⁹ and II-VI⁴⁰. Therefore, the unconventionally high speed makes condensed excitons in direct-bandgap monolayer MoS₂ the fastest excitation in electronic matter observed in a solid-state system.

Within Keldysh's framework^{1,4}, the group velocity of condensed excitons follows the hydrodynamic relation $v_{X,L} \propto \sqrt{f}$, where f characterizes the many-body interactions within the Bose-Fermi gas mixture. To stabilize the condensate against disorder and the formation of charged excitons, biexcitons and electron-hole droplets, f takes real positive values. In monolayer MoS₂, $f = f(T, V_g)$ depends on temperature and V_g , and defines the phase diagram in Fig. 2(D). With increasing f , the exciton liquid expands through the two-dimensional crystal with remarkably large speed $v_{X,L}$, suggesting a frictionless, or superfluid flow of condensed excitons.

The unconventionally strong repulsions among excitons causes a significant blue-shift of the exciton feature in the pump-on with respect to the pump-off raw reflectance spectra (Figs. S17-S18). We estimate the net repulsive energy ΔE_{X-X} arising from exciton-exciton interactions, which is shown in Fig. 4(B) for $\Delta t = 2.4$ ps. In the range 0-5 μm , ΔE_{X-X} has the largest value of ~ 3 meV, comparing well to that of dipolar indirect excitons¹¹ and polaritons³² condensates. ΔE_{X-X} follows the decay of the exciton population given by $DR(x, E_X(0))$

(solid-pink curve) that decreases slowly to ~ 1 meV far from the laser spot.

In conclusion, we have realized the condensation of ultrashort-lived excitons in a direct-bandgap, atomically-thin MoS₂ semiconductor. The condensation resulting from many-body interactions within the mixture of Bose (excitons) and Fermi (free-carriers) gases, controlled by an electrical backgate, takes place when exciton-exciton repulsions dominate over exciton-electron attractions and remains stable until $T_c \sim 150$ K. The exciton liquid propagates over long-distances (at least 60 micrometers) with record velocity of $\sim 1.8 \times 10^7$ m/s ($\sim 6\%$ the speed of light). Our findings have implications in high-temperature superconductivity, excitonic circuitry and spin-valley Hall devices mediated by excitonic superfluids for the next-generation quantum-technologies by using semiconducting monolayers.

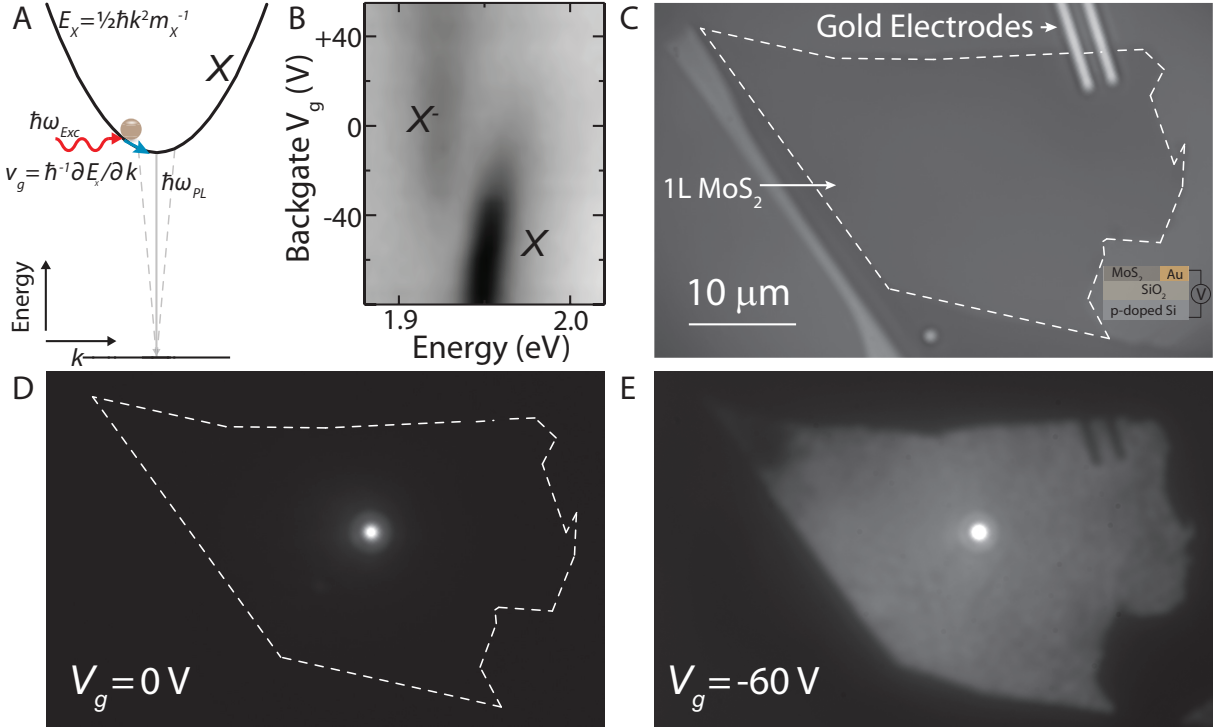


Fig. 1: Exciton condensation driven by an electrical-backgate in an atomically-thin MoS₂ semiconductor. (A) Parabolic exciton dispersion $E_X(k_X)$ (black curve). A dilute exciton gas is generated using near-resonance excitation (red wavy-arrow) with energy $\hbar\omega_{\text{Exc}}$, propagates with small group velocity $v_X(k_X) = \hbar^{-1}\partial E_X(k_X)/\partial k_X$ (blue-arrow) and finally radiatively recombine within the light cone (dashed-line) with energy $\hbar\omega_{\text{PL}}$ (gray solid-line). (B) Reflectance contrast showing the charged (X^-) and neutral (X) exciton resonance energy as a function of photon energy and backgate V_g . (C) Optical image of an electrically contacted monolayer with large area of $\sim 1200 \mu\text{m}^2$. The sample contour is highlighted by the dashed-line. Right-bottom inset: Device schematic. Low-temperature (20 K) spatially-resolved photoluminescence images at (D) $V_g = 0 \text{ V}$ and (E) -60 V . All images have been taken using the same magnification.

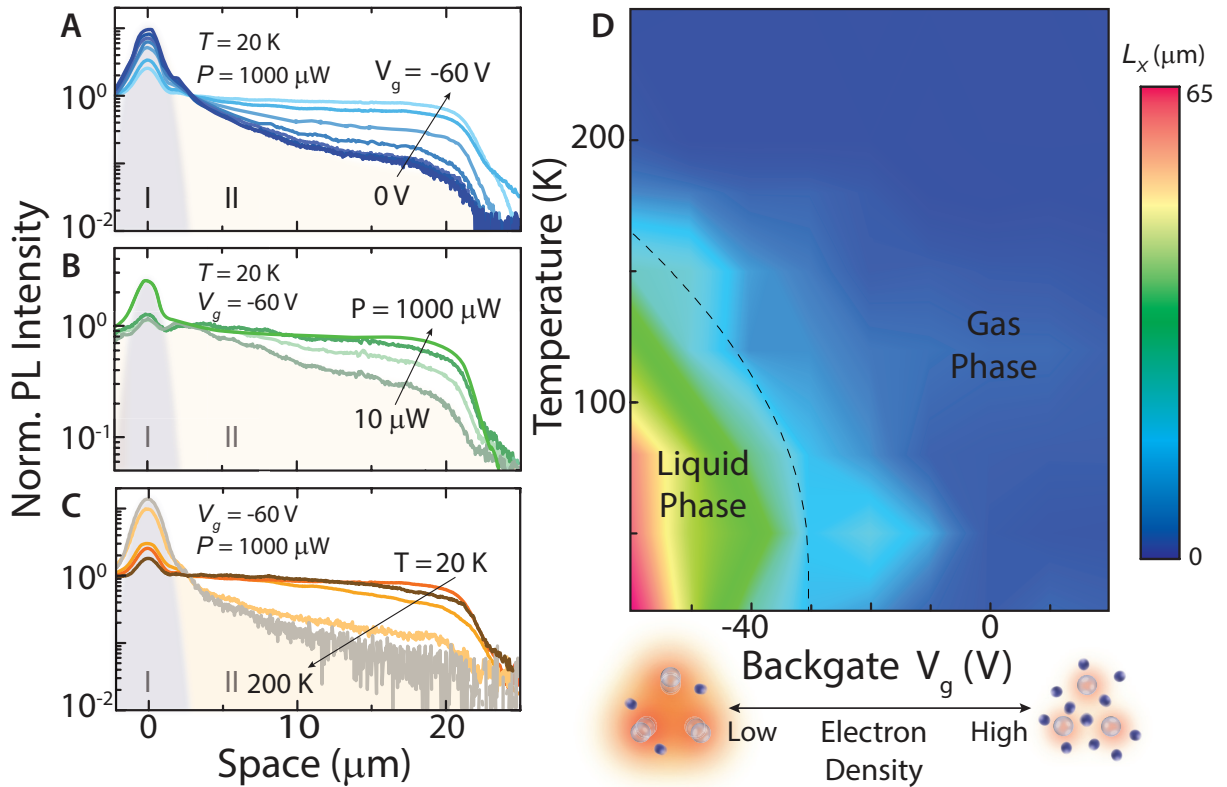


Fig. 2: Exciton phase diagram. Spatial cross-section profiles in a semilogarithmic scale of the photoluminescence images as a function of (A) backgate, where V_g varies from 0 V (bottom curve) to -60 V (top curve) with a step of -10 V, taken at fix $P = 1000 \mu\text{W}$ and $T = 20 \text{ K}$; (B) power, where $P = 10 \mu\text{W}, 50 \mu\text{W}, 100 \mu\text{W}$ and $1000 \mu\text{W}$ from bottom to top, taken at fix $V_g = -60 \text{ V}$ and $T = 20 \text{ K}$; (C) temperature, where $T = 200 \text{ K}, 180 \text{ K}, 150 \text{ K}, 80 \text{ K}$ and 20 K from bottom to top, taken at fix $P = 1000 \mu\text{W}$ and $V_g = -60 \text{ V}$. The sharp drop of the PL intensity in (A), (B) and (C) corresponds to the monolayer edge. All spectra have been normalized to the maximum intensity of the exponential distribution for easy comparison among experiments. (D) Phase diagram of the fluid transport length $L_x(V_g, T)$. The liquid (gas) phase domain, where the electron density is low (high), occupies the left-side (right-side) of the dashed guideline. The scale bar is given. Illustration: At low (high) electron (solid-dark spheres) density, excitons (transparent-light spheres) experience strong (weak) collective repulsions causing exciton condensation and propagation over long distances.

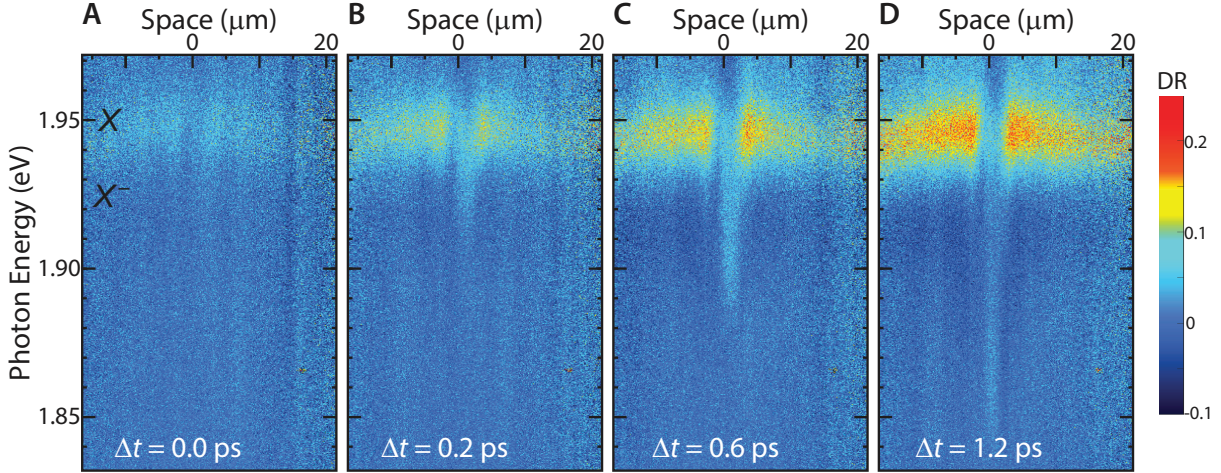


Fig. 3: Transport of condensed excitons. Spatially- (horizontal-axis) and energy-resolved (vertical-axis) differential reflectance ($DR(x, E)$) at delay times (Δt) of (A) 0 ps, (B) 0.2 ps, (C) 0.6 ps and (D) 1.2 ps, measured at fixed conditions $T = 20$ K, $V_g = -60$ V and $n_X \sim 1.7 \times 10^{12} \text{ cm}^{-2}$. $DR(x, E)$ is defined as $[R_{\text{On}}(x, E) - R_{\text{Off}}(x, E)]/R_{\text{Off}}(x, E)$, where $R_{\text{On}}(x, E)$ and $R_{\text{Off}}(x, E)$ are the reflectance profiles with the pump on and off, respectively. The positive (negative) $DR(x, E)$ signal indicates strong (weak) reflectance, corresponding to pump-induced photobleaching (pump-induced absorption) of a state at energy E at position x . The spot of the pump laser is located at the center of the monolayer ($x = 0 \mu\text{m}$). The photobleaching at the exciton resonance propagates 20 μm after a pump-probe delay of $\Delta t = 1.2$ ps, clearly demonstrating the unconventionally high propagation speed of condensed excitons of the order of 10^7 m/s.

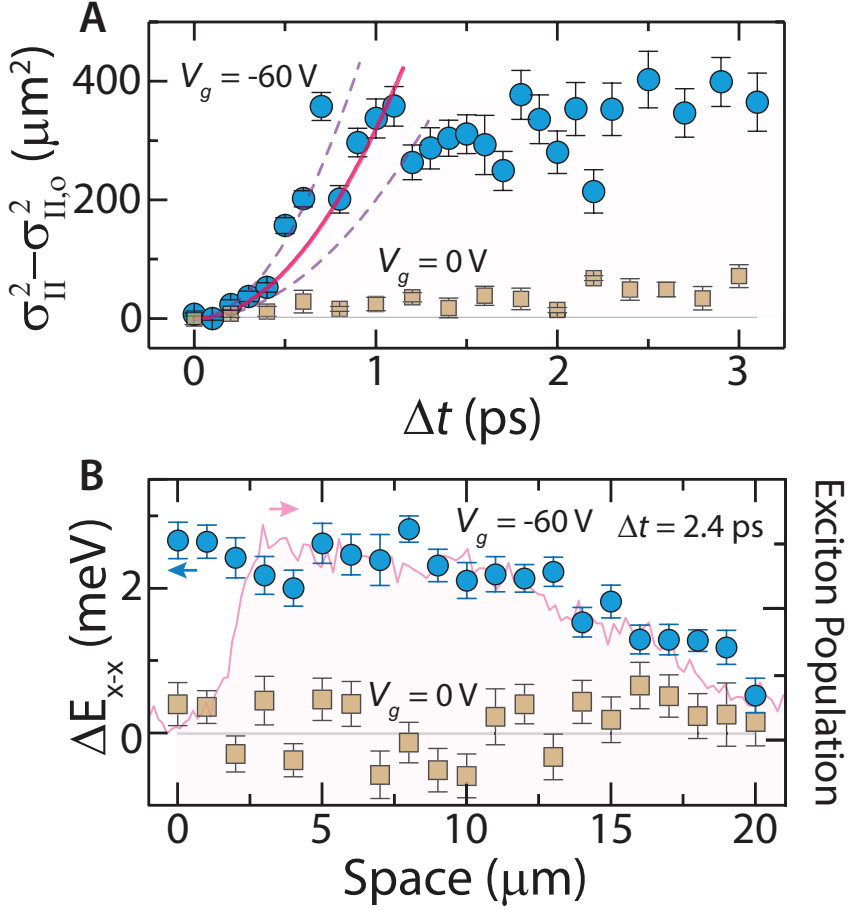


Fig. 4: Non-linear transport and energy blueshift (repulsive interaction) of condensed excitons. (A) Temporal-evolution of the mean-square-displacement (MSD) $\sigma_{\text{II}}^2 - \sigma_{\text{II},0}^2$ as a function of Δt for excitons at the liquid (blue circles, $V_g = -60 \text{ V}$) and gas (purple squares, $V_g = 0 \text{ V}$) phase. The quadratic behaviour of the MSD is reproduced (red curve) by using a power law $\sigma_{\text{II}}^2 - \sigma_{\text{II},0}^2 = v_{X,L}t^\alpha$ with $\alpha = 2$, which demonstrates the ballistic-like propagation of the exciton liquid. The liquid speed $v_{X,L} = (1.8 \pm 0.3) \times 10^7 \text{ m/s}$. Dashed-lines represent upper and lower limits of the MSD fitting, which provides the uncertainty of $v_{X,L}$. (B) Energy change of excitons $\Delta E_{\text{X-X}}$ at the liquid (blue circles, $V_g = -60 \text{ V}$) and gas (purple squares, $V_g = 0 \text{ V}$) phase as a function of position x . Large blueshifted energy (positive $\Delta E_{\text{X-X}}$) is detected in the liquid phase, due to the strong repulsive exciton-exciton interaction, while no net repulsion is observed at the gas phase ($\Delta E_{\text{X-X}} \sim 0$). $\Delta E_{\text{X-X}}$ decreases as exciton liquid propagates in space following the decrease in the density (solid-pink curve, right axis).

Methods

Device Fabrication

Large MoS₂ monolayers with the typical long side of 40 to 60 μm and area of \sim 1200 μm^2 were mechanically exfoliated from natural bulk MoS₂ crystals onto a polydimethylsiloxane (PDMS) stamp. The MoS₂ monolayers were then carefully transferred from the PDMS stamp onto clean 285 nm SiO₂/Si p-type dry oxide substrates, ensuring that smooth, uncracked large area monolayers are obtained upon transfer. The successful transfers were verified under an optical microscope by optical contrast. A poly(methyl methacrylate) (PMMA) mask was spin coated on the substrates and patterned electrical contact areas were defined on the mask by standard electron beam lithography. 5 nm Cr/ 50 nm Au electrical contacts were subsequently deposited by thermal evaporation. The final devices were obtained after an acetone lift-off procedure. To control the electron concentration of the MoS₂ devices in our optical experiments, a backgate voltage was applied to the Si substrate and the MoS₂ monolayers grounded via the electrical contacts.

Optical Imaging and Experimental Setup

The fabricated devices were mounted on a cold finger cryostat and cooled down using a continuous flow of liquid helium. The cryostat station was mounted on the photoluminescence (PL) and transient reflectance (TR) imaging setup that operated in two different imaging configurations (see SI for details).

In the PL imaging configuration, the samples were excited with a He-Ne (632.8 nm) continuous wave (cw) laser cleaned by an interference filter resonant with the A-exciton of the MoS₂ monolayer. Using a 50 \times objective lens (NA = 0.55), the laser was focused to locally excite a small spot with diameter of 1.5 μm on the large sample. The objective then collected the PL emission. An ultra-steep-edge long pass filter placed in the detection path before the

optical detector removes reflected laser light, allowing only PL image signal to be measured. A set of lenses were added in the detection path to change the image magnification and effective field of view on the optical detector (sCMOS sensor). This enables imaging to be optimized for samples of different sizes. The sCMOS chip has an area of 2300×2300 pixels, $6.5 \mu\text{m}$ each. Our detection system provides a high spatial resolution of 40 nm per pixel in either axial direction.

For TR imaging, a femtosecond pulsed pump laser (615 nm) is used to excite the sample. A pulsed broadband white light beam given a time delay Δt with respect to the pump is used to probe the changes in the reflectance of the sample in the visible (625 – 700 nm) region. The size of the probe beam illuminating the sample surface is controlled by a series of lenses, which focuses the probe at the back focal plane of the objective lens to maximize the probe and cover the entire sample. The reflected probe beam was collected by the same objective and dispersed by a single grating (600 gr/mm) monochromator with 550 mm of focal length and the signal was detected by a scientific CCD detector cooled with liquid-nitrogen. Energy-space reflectance spectrum map images are measured for each time delay under pump on/off conditions. As the technique relays in the changes in the optical reflectance/absorption, the dynamics of the exciton population within the light-cone, which includes the spatial propagation, radiative recombination and relaxation into other states, is monitored in great detail.

1. Keldysh, L. V. & N., K. A. Collective properties of excitons in semiconductors. *Soviet Physics JETP* **27**, 978–993 (1968).
2. Anderson, M. H., Ensher, J. R., Matthews, M. R., Wieman, C. E. & Cornell, E. A. Observation of bose-einstein condensation in a dilute atomic vapor. *Science* **269**, 198–201 (1995).

3. Davis, K. B. *et al.* Bose-einstein condensation in a gas of sodium atoms. *Phys. Rev. Lett.* **75**, 3969–3973 (1995).
4. Koinov, Z. G. Bose-einstein condensation of excitons in a single quantum well. *Phys. Rev. B* **61**, 8411–8419 (2000).
5. Keldysh, L. V. The electronhole liquid in semiconductors. *Contemp. Phys.* **27**, 395428 (1986).
6. Deng, H., Haug, H. & Yamamoto, Y. Exciton-polariton bose-einstein condensation. *Rev. Mod. Phys.* **82**, 1489–1537 (2010).
7. Butov, L. V., Gossard, A. C. & Chemla, D. S. Macroscopically ordered state in an exciton system. *Nature* **418**, 751754 (2002).
8. Snoke, D., Denev, S., Liu, Y., Pfeiffer, L. & West, K. Long-range transport in excitonicdark states in coupled quantum wells. *Nature* **418**, 754 (2002).
9. Tutuc, E., Shayegan, M. & Huse, D. A. Counterflow measurements in strongly correlated gaas hole bilayers: Evidence for electron-hole pairing. *Phys. Rev. Lett.* **93**, 036802 (2004).
10. Eisenstein, J. P. & MacDonald, A. H. Boseeinsteinc condensation of excitons in bilayer electron systems. *Nature* **432**, 691694 (2004).
11. Stern, M., Umansky, V. & Bar-Joseph, I. Exciton liquid in coupled quantum wells. *Science* **343**, 55–57 (2014).
12. Cohen, K., Shilo, Y., West, K., Pfeiffer, L. & Rapaport, R. Dark high density dipolar liquid of excitons. *Nano Letters* **16**, 3726–3731 (2016).

13. Wang, Z. *et al.* Evidence of high-temperature exciton condensation in two-dimensional atomic double layers. *Nature* **574**, 76–80 (2019).
14. Korn, T., Heydrich, S., Hirmer, M., Schmutzler, J. & Schller, C. Low-temperature photo-carrier dynamics in monolayer mos2. *Applied Physics Letters* **99**, 102109 (2011).
15. Robert, C. *et al.* Exciton radiative lifetime in transition metal dichalcogenide monolayers. *Phys. Rev. B* **93**, 205423 (2016).
16. Liu, S. *et al.* Room-temperature valley polarization in atomically thin semiconductors via chalcogenide alloying. *ACS Nano* **14**, 9873–9883 (2020).
17. Steinhoff, A. *et al.* Exciton fission in monolayer transition metal dichalcogenide semiconductors. *Nat. Commun.* **8**, 1166 (2017).
18. Kumar, N. *et al.* Exciton diffusion in monolayer and bulk mose2. *Nanoscale* **6**, 4915–4919 (2014).
19. Kato, T. & Kaneko, T. Transport dynamics of neutral excitons and trions in monolayer ws2. *ACS Nano* **10**, 9687–9694 (2016).
20. Onga, M., Zhang, Y., Ideue, T. & Iwasa, Y. Exciton hall effect in monolayer mos2. *Nat. Mat* **16**, 11931197 (2017).
21. Zipfel, J. *et al.* Exciton diffusion in monolayer semiconductors with suppressed disorder. *Phys. Rev. B* **101**, 115430 (2020).
22. Glazov, M. M. Quantum interference effect on exciton transport in monolayer semiconductors. *Phys. Rev. Lett.* **124**, 166802 (2020).

23. Hotta, T. *et al.* Exciton diffusion in *h*BN-encapsulated monolayer MoSe₂. *Phys. Rev. B* **102**, 115424 (2020).
24. Uddin, S. Z. *et al.* Neutral exciton diffusion in monolayer mos2. *ACS Nano* **14**, 13433–13440 (2020).
25. Lai, C. W., Zoch, J., Gossard, A. C. & Chemla, D. S. Phase diagram of degenerate exciton systems. *Science* **303**, 503–506 (2004).
26. Efimkin, D. K., Laird, E. K., Levinsen, J., Parish, M. M. & MacDonald, A. H. Electron-exciton interactions in the exciton-polaron problem. *Phys. Rev. B* **103**, 075417 (2021).
27. Shahnazaryan, V., Iorsh, I., Shelykh, I. A. & Kyriienko, O. Exciton-exciton interaction in transition-metal dichalcogenide monolayers. *Phys. Rev. B* **96**, 115409 (2017).
28. Kosuke Yoshioka, E. C. & Kuwata-Gonokami, M. Transition to a boseeinstein condensate and relaxation explosion of excitons at sub-kelvin temperatures. *Nat. Commun.* **2**, 328 (2011).
29. Fogler, M. M., Butov, L. V. & Novoselov, K. S. High-temperature superfluidity with indirect excitons in van der waals heterostructures. *Nat. Commun.* **5**, 4555 (2014).
30. Amani, M. *et al.* Near-unity photoluminescence quantum yield in mos2. *Science* **350**, 1065–1068 (2015).
31. Lien, D.-H. *et al.* Electrical suppression of all nonradiative recombination pathways in monolayer semiconductors. *Science* **364**, 468–471 (2019).
32. Ballarini, D. *et al.* Macroscopic two-dimensional polariton condensates. *Phys. Rev. Lett.* **118**, 215301 (2017).

33. Michalsky, T., Wille, M., Grundmann, M. & Schmidt-Grund, R. Spatiotemporal evolution of coherent polariton modes in zno microwire cavities at room temperature. *Nano Letters* **18**, 6820–6825 (2018).
34. D.C.Elias *et al.* Dirac cones reshaped by interaction effects in suspended graphene. *Nat. Physics* **7**, 701704 (2011).
35. Baringhaus, J. *et al.* Exceptional ballistic transport in epitaxial graphenenanoribbons. *Nature* **506**, 349 (2014).
36. Guo, Z. *et al.* Long-range hot-carrier transport in hybrid perovskites visualized by ultrafast microscopy. *Science* **356**, 59–62 (2017).
37. Sung, J. *et al.* Long-range ballistic propagation of carriers in methylammonium lead iodide perovskite thin films. *Nat. Physics* **16**, 171176 (2020).
38. Sanvitto, D. *et al.* Observation of charge transport by negatively charged excitons. *Science* **294**, 837–839 (2001).
39. Trauernicht, D. P., Wolfe, J. P. & Mysyrowicz, A. Highly mobile paraexcitons in cuprous oxide. *Phys. Rev. Lett.* **52**, 855–858 (1984).
40. Kalt, H. *et al.* Quasi-ballistic transport of excitons in quantum wells. *Journal of Luminescence* **112**, 136–141 (2005).

Data availability

All methods and data generated and/or analyzed supporting the findings of this study are included in this paper and its Supplementary Information file and are available from the corresponding authors upon reasonable request.

Acknowledgments

Q.X. gratefully acknowledges strong support from the State Key Laboratory of Low-Dimensional Quantum Physics and start-up grant from Tsinghua University. M.B. gratefully acknowledges the support from the Nanyang Technological University for the NAP-SUG grant. X.L. gratefully acknowledges the financial support from the National Natural Science Foundation of China (12104006). A.G.D.A gratefully acknowledges the financial support from the Singapore Ministry of Education via AcRF Tier3 Programme Geometrical Quantum Materials (MOE2018-T3-1-002) and from the Presidential Postdoctoral Fellowship program of the Nanyang Technological University. We acknowledge Prof. T.C.H. Liew and Dr. A. Álvarez Fernández for fruitful discussions.

Author contributions

A.G.D.A. and Q.X. started the project. A.G.D.A. conceived and designed the experiments. Y.R.W and X.L. designed and fabricated the large area devices. A.G.D.A, Y.R.W, X.L. and A.F. performed the experiments. Q.X., M.B., Y.R.W. and T.T.H.D. intensively discussed the results and the manuscript during its preparation. A.G.D.A analyzed and interpreted the data and wrote the manuscript with the help of all co-authors. A.G.D.A and Y.R.W contributed equally to this work.

Competing interests

The authors declare no competing interests

Supplementary Information

A supporting information file with information regarding sample fabrication, experimental details, analysis, fitting procedures, theoretical section and additional data supporting the main findings of the main manuscript file is available.

Supplementary Files

This is a list of supplementary files associated with this preprint. Click to download.

- [SupportingVideo.mp4](#)
- [GranadosSupportingInformation.pdf](#)